Mesoscopic simulations of a fracture process in reinforced concrete beam in bending using a 2D coupled DEM/ micro-CT approach

Michał Nitka , Jacek Tejchman

Faculty of Civil and Environmental Engineering, Gdańsk University of Technology, Narutowicza Street 11/12, 80-233 Gdansk, Poland

A B S T R A C T

In this study, a complex fracture process in a short rectangular concrete (RC) beam reinforced by one longitudinal bar (without vertical reinforcement) and subjected to quasi-static three-point bending was numerically explored in 2D conditions. A critical diagonal shear crack in the beam caused it to fail during the experiment. The numerical simulations were conducted with a classical particle discrete element method (DEM). A three-phase concrete description (aggregate, mortar, and interfacial transitional zones (ITZs) around aggregates) accounted for the concrete heterogeneity. In mesoscopic DEM calculations based on a 2D X-ray CT scan, the actual shape and placement of aggregate particles in concrete were taken for granted. In the study, the steel bar with ribs was replicated. ITZ was also assumed between the bar and mortar. Without imposing any bond-slip law, a geometrical bar/concrete interface condition was explicitly considered. The focus was on the force–deflection diagram, fracture process, contact forces, and stresses along the bar. A good level of agreement about the evolution of the vertical force versus the deflection and failure mechanism was attained between DEM analyses and in-house laboratory tests despite simplified 2D conditions. A strong effect of concrete mesostructure on the crack pattern was found.

1. Introduction

Concrete is the most often used composite building material in the world in terms of volume because it is simple to make and has the lowest cost-to-strength ratio when compared to other building materials. It has a high compressive strength despite possessing low tensile strength and ductility. Low tensile strength makes concrete materials susceptible to cracks under static and dynamic loads. Cracks are a fundamental phenomenon in concrete [1–4]. A good understanding of crack formation and propagation is crucial for the assessment of structural optimization and concrete safety. The heterogeneous concrete structure, which can range in length from a few nanometers (hydrated cement) to millimeters (aggregate particles), greatly influences a fracture process. The aggregate size, shape, roughness, distribution, and volume, as well as mortar porosity, are the main determining elements [3–7]. Concrete can be divided into mortar, aggregate, interfacial transition zones (ITZs), and macro-voids when analyzed at the mesoscale [5]. Porous ITZs around aggregates at a specific distance of 0.015–0.100 mm [8–10] are substantially weaker than aggregate and mortar and have higher permeability, diffusivity, and conductivity [11–13]. Thus, they operate as attractors for the growth of microcracks and should therefore be modeled at the mesoscale to accurately represent a fracture process [14–16]. Mesoscale modeling has the advantage that it

---

Nomenclature

a	shear span
B	beam width
C	cohesive contact stress
d	particle diameter
E	Young's modulus
E_c	Young's modulus of particle contact
f_i^c	contact force
f_c	compressive strength of concrete
f_t	tensile strength
f_y	yield stress
F	global vertical force
F_{min}^n	minimum tensile contact force
F_{max}^s	critical cohesive contact force
F_n	normal contact force
F_s	tangential contactforce
H	beam height
K_n	normal contact stiffness
K_s	tangential contact stiffness
l^c	distance between two centers of elements in contact
L	beam length
N	number of broken contacts
p	porosity
R	particle radius
T	tensile normal contact stress
u	deflection
u_s	slip
U	overlap between discrete elements
v	velocity
V	shear strength
w	width
α_d	damping parameter
ε	normal strain
μ_c	inter-particle friction angle
ν	Poisson's ratio
ν_c	Poisson's ratio of particle contact
ρ	particle mass density
ρ_r	reinforcement ratio
σ	normal stress
σ_w	wall normal stress
τ_w	wall shear stress
CMOD	crack mouth opening displacement
CT	computed tomography
DEM	discrete element method
ITZ	interfacial transition zone
2D	two-dimensional
'a'	aggregate
'bond'	bond
'cm'	cement matrix
'damp'	damped
'max'	maximum
'min'	minimum
'p'	particle

may be used to thoroughly examine the mechanism of the initiation, growth, and formation of localized zones and cracks that significantly affect the behavior of concrete at the macroscopic level. Concrete fracture at the mesoscale may be realistically replicated with 1) continuous and discontinuous finite element (FE) models [3,17–24], based on various constitutive laws (elasto-plastic, damage, coupled elasto-plastic-damage, phase field ones), or using cohesive elements, and 2) discrete models [25–31]. The most
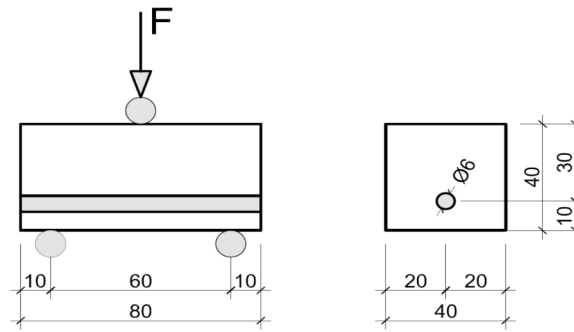
Fig. 1. Geometry of short concrete beam reinforced with one longitudinal steel ribbed bar (dimensions are given in [mm]) [51].

popular discrete approach is the classical particle discrete element method (DEM) [27,29,30,32–35]. The other discrete models are interface element models with constitutive laws based on non-linear fracture mechanics [26], lattice methods [25,28,37], rigid-body-spring models [38–40], and lattice discrete particle approaches [41–43]. One of its drawbacks is that mesoscopic models are difficult to apply to industrial-scale engineering problems due to the long computation times resulting from a large number of particles. As a result, mesoscopic models cannot take the place of macroscopic continuum models in numerical analyses and should not be directly applied to calculations involving large concrete and RC elements. The significant results of those mesoscale simulations may help to enhance macroscale continuum models since they are more realistic in fracture process simulations.

The mechanical behavior of RC structures is significantly influenced by the bond strength between reinforcement and concrete. The stress transfer between those two materials is caused mainly by adhesion, mechanical interaction, and friction. The steel reinforcement roughness, aggregate size, concrete cover, concrete's compressive strength, bar yield stress, bar diameter, and lateral confinement have the most effects on RC elements' bond strength [3,44–46]. In the literature, several bond-slip rules between concrete and reinforcement were suggested, based on laboratory experiments (e.g. [47–50]). In general, they are reliant on the boundary conditions of the entire system. Thus, there are no universal slip-bond laws for RC elements. In addition, it is impossible to investigate the mesomechanical failure mechanism of the bond between steel bars and concrete with the use of slip-bond laws.

The research work being discussed is numerically oriented and concerns a simply supported short reinforced concrete (RC) beam with one steel ribbed bar under 3-point bending that was earlier tested at the laboratory scale [51]. The beam was designed to fail due to shear because it was over-reinforced, had a low depth-to-shear span ratio, and lacked vertical shear reinforcement. The crack pattern included one critical diagonal shear crack with some secondary cracks. The force–deflection curve exhibited both softening and re-hardening. The numerical simulations were carried out at the mesoscale using the classical particle discrete element method (DEM). The beam material was modeled as an assembly of individual particles that could move independently within the domain and interact. We chose DEM over other discrete models because it has the potential to accurately depict a concrete fracture process [5–7,33,34]. Additionally, it accurately represents material mesostructure and contact forces by using straightforward dynamic equations. Particularly, the DEM model offers incredibly accurate fracture findings when the mesostructure is taken into account in 3D simulations based on micro-CT images [5,7,34]. Three different phases were distinguished in concrete in the DEM analyses that covered aggregate, mortar, and interfacial transitional zones (ITZs) adjacent to aggregate particles. Based on X-ray CT scans, the actual shape and placement of aggregate particles in concrete were taken for granted. To simulate aggregates, a clumped-particle geometry was employed. ITZs were assumed to be 0-thick. The use of such a simple representation of ITZ is usually sufficient in calculations [5,7] although the assumption of ITZs of a defined width provides more accurate outcomes [6]. In simulations, the bar/concrete interface was explicitly reproduced. The steel bar was modeled by taking directly its ribs into account. Moreover, ITZ was added between the mortar and steel [52]. Thus, DEM simulations for the RC beam used a 5-phase material. In the computations, the force–deflection curve, fracture process, contact forces, and stresses along the steel bar were carefully studied. The preceding experiment [51] and the 2D numerical results (load–deflection diagram and fracture formation) were directly compared. Furthermore, the DEM outcomes utilizing the real mesostructure were juxtaposed with those utilizing the artificial one.

The motivation for the current numerical mesoscopic simulations were two interesting phenomena occurring during the laboratory test [51]: 1) the occurrence of the rehardening phase during deformation and 2) a complex pattern of secondary cracks. The first phenomenon cannot be reproduced by macroscopic continuum models [53] without the artificial assumption of material rehardening. The second one requires the consideration of internal imperfections by the assumption of the actual concrete mesostructure and the shape of the steel bar.

In the current study, the novel research aspect was an in-depth numerical investigation of a complex fracture process at the aggregate level in a short reinforced concrete beam under quasi-static 3-point bending by taking the actual mesostructure of concrete and steel bar shape into account, based on a coupled DEM/micro-CT approach. This coupled approach was not used for RC elements. In the simulations, a geometric interface between the concrete and steel bar was assumed to prevent the reliance of bond-slip rules on the boundary conditions of the entire system. A bond-slip relationship was not thus imposed in DEM simulations; it was the outcome of them. In the first step, 2D simulations were performed. There exist already numerical mesoscopic simulations within continuum mechanics wherein ribs on the surface of rebars were explicitly taken into account [54,55]. However, in numerical modelling of the interface between concrete and reinforcement, the bond-slip laws are usually assumed. This DEM study has also some limitations,
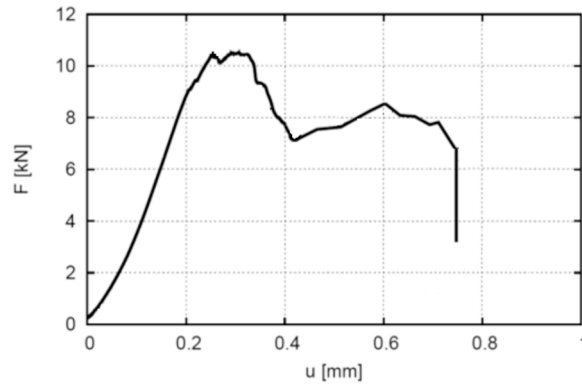
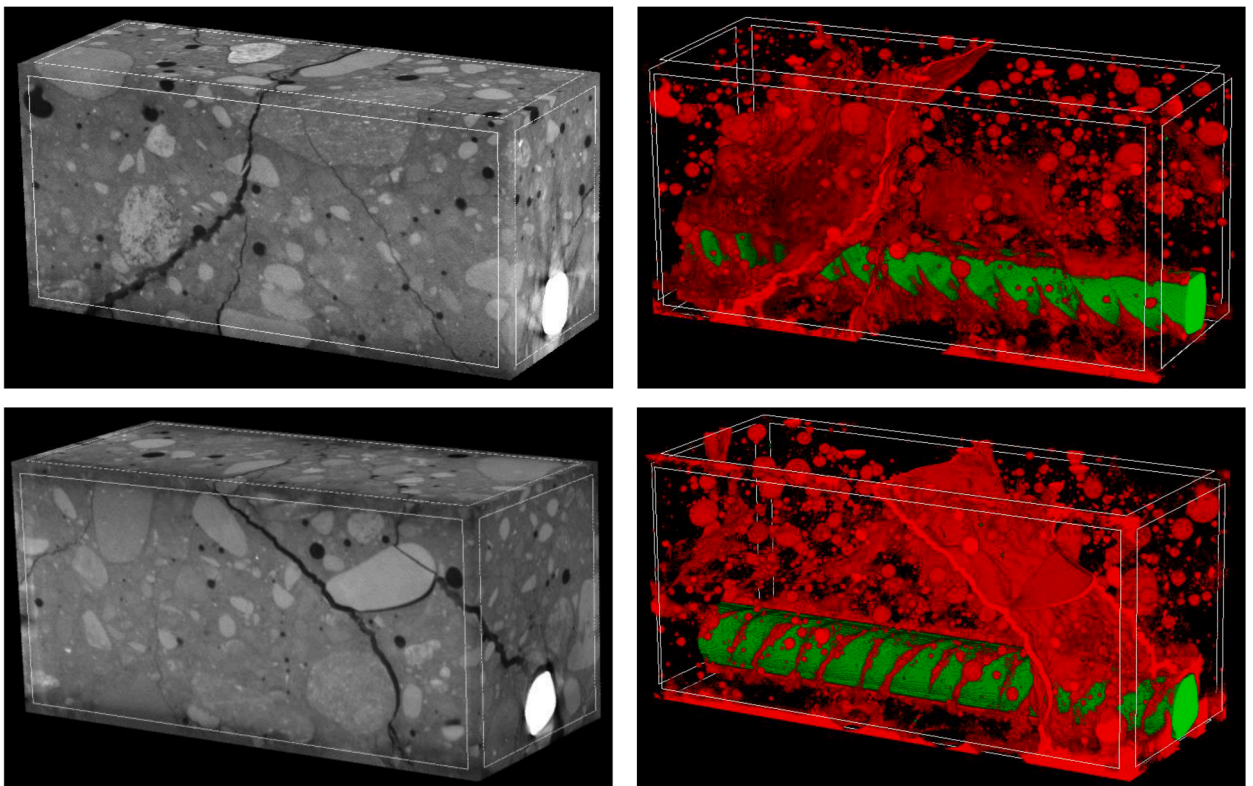Fig. 2. Experimental force–deflection curve F = f(u) for short RC beam with steel bar [51].

Fig. 3. 3D micro-CT images of short RC beam reinforced with steel ribbed bar on both sides at failure (pores and cracks are in red, steel bar is in green) [51].

including 2D simulations (the spatial interference of cracks surrounding the bar was thus ignored), simplified 0-wide ITZs around both aggregates and a steel bar, disregarded macro-pores, and the absence of aggregate fragmentation in the concrete mesostructure. The 2D simulations were carried out for a beam cross-section with a steel bar. DEM simulations were performed using the YADE open-source software [56,57].

There are many DEM solutions for concrete. For RC elements, on the other hand, DEM is far less common. The existing studies (e.g. [58–61]) confirm that DEM may be also reliably used to examine a fracture process in RC elements

2. Experiments

Laboratory tests were extensively detailed in [51]. The length of the rectangular RC beam with one longitudinal steel bar was $L = 80$ mm, and its height and width were $H = B = 40$ mm (Fig. 1). The effective height was $D = 30$ mm, and the effective depth-to-shear
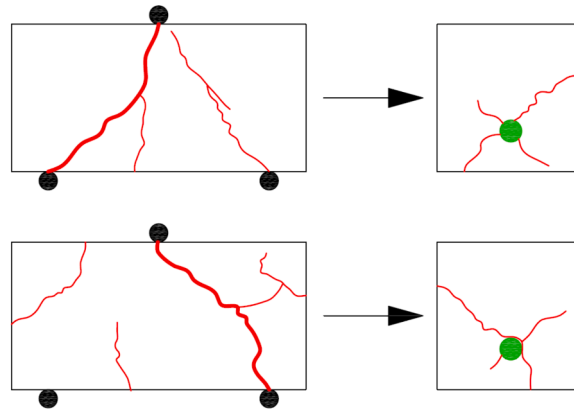
Fig. 4. Sketch of final crack pattern for short RC beam on all 4 sides (critical shear crack is marked as thick red line, and reinforcement is marked in green) [51].
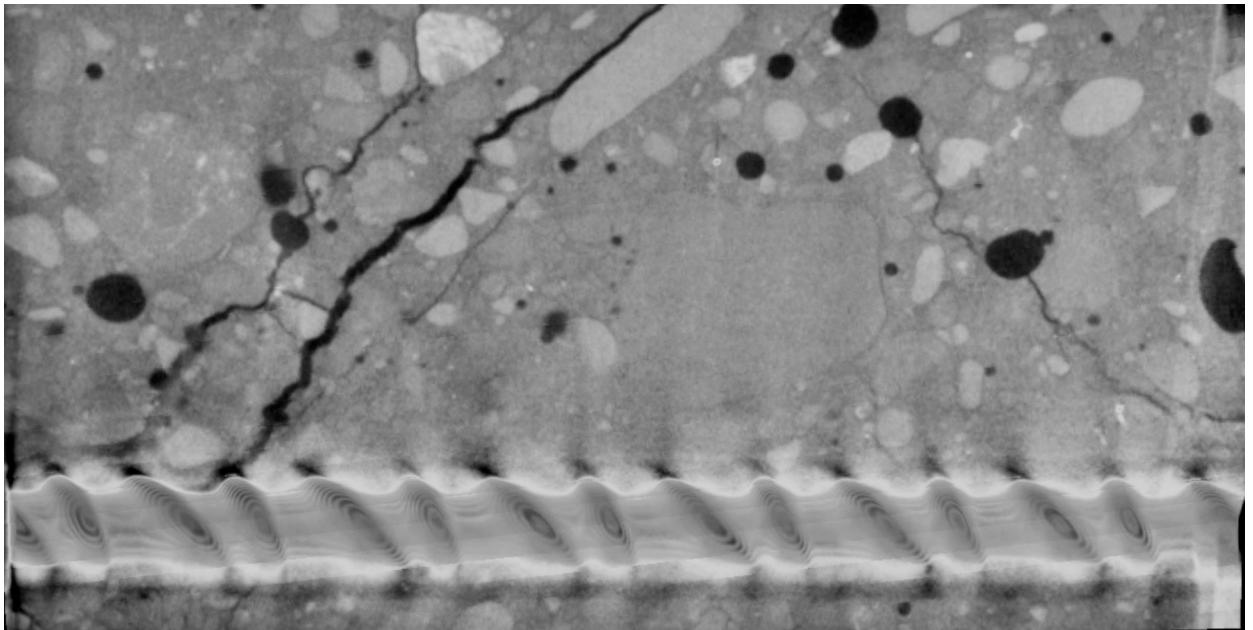

Fig. 5. Crack pattern in RC beam from 2D micro-CT image in vertical beam mid-plane crossing ribbed bar (black spoths denote macro-pores).

span ratio was $a/D = 1.0$. The usage of a single, 6 mm-diameter steel bar was made. The reinforcement ratio was high $\rho_r = 1.8$ % to avoid bar yielding. No vertical reinforcement was used. Bar's ribs had a height of $h_r = 0.7$ mm and spacing $h_s = 6$ mm. The reinforcement's mechanical characteristics were as follows: steel had a tensile strength of 650 MPa while having an elasticity modulus of 200 GPa. Round aggregate particles with a maximum diameter of 16 mm were used in concrete. Sand and aggregate particles had an average diameter of $d_{50} = 2$ mm ($>h_r$). A short concrete beam with a steel bar had an initial pore volume of $p = 2.7$ %. Concrete's average uniaxial compressive strength was $f_c = 49.75$ MPa, Young's modulus was $E = 34.8$ GPa, and Poisson's ratio was $\nu = 0.21$ on average. The average tensile strength during bending was $f_t = 3.96$ MPa. The concrete cover was 7 mm. With a displacement-controlled option (CMOD) and a rate of 0.002 mm/min, laboratory testing was conducted. The micro-CT apparatus mounted on the Instron 5569 loading machine was used to constantly scan the beam [51].

Fig. 2 depicts the evolution of the vertical force versus the beam deflection $F = f(u)$. The beam's highest vertical force was 10.46 kN. The greatest force's associated deflection was $u = 0.26$ mm. Flexural strength was 14.71 MPa whereas shear strength, $V = F/bD$, was 8.72 MPa. Unexpected re-hardening was seen between deflections $u = 0.4$–0.6 mm, according to the force–deflection diagram. The beam failed at $u = 0.75$ mm. Images of the beam at failure are presented in Fig. 3 from two different views.

The beam failed in shear due to three factors: a) a high reinforcement ratio of $\rho_r = 1.8$ %, b) a low effective depth-to-shear span ratio of $a/D = 1.0$, and c) a lack of vertical reinforcement [62] Based on images of both beam sides (Fig. 3), the diagonal critical shear crack between the beam support and loading point caused the beam to collapse in a quick brittle manner. Before the beam failure, a few
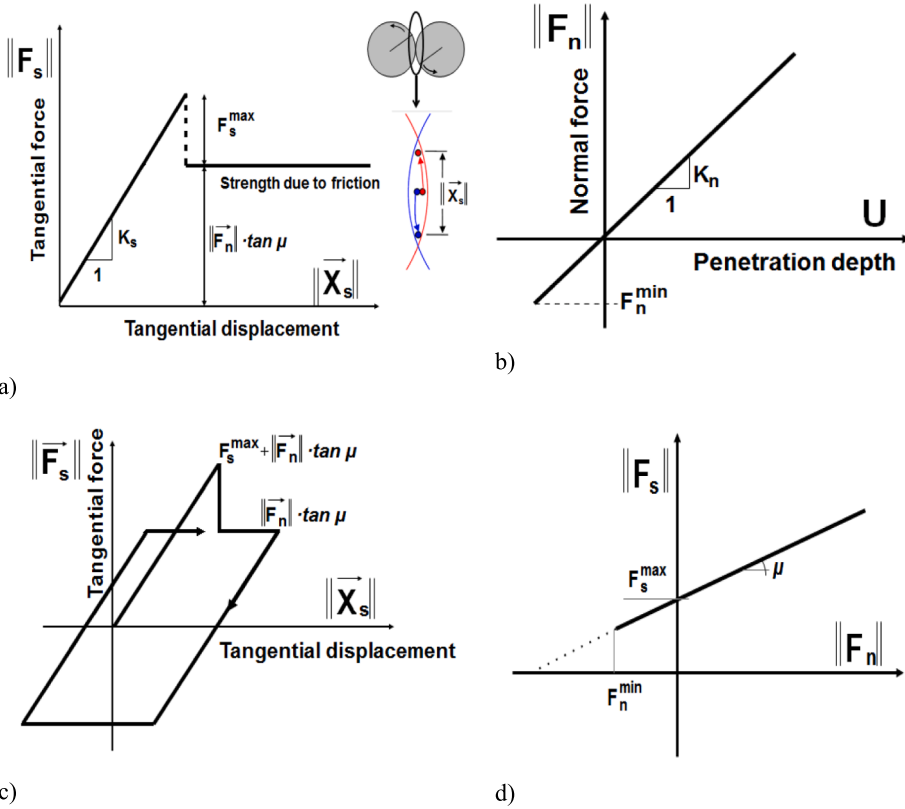
Fig. 6. Mechanical response of DEM: a) tangential contact model, b) normal contact model, c) loading and unloading path in tangential contact model and d) modified Mohr-Coulomb model [5,6,56,57].

secondary cracks could also be observed (Fig. 4).

The 2D micro-CT image in the vertical beam mid-plane crossing the bar is shown in Fig. 5 (chosen for DEM simulations). The crack pattern was extremely intricate. In addition to the critical inclined shear crack on the left beam side (under $\cong 45°$ to the horizontal), two secondary cracks were also apparent: the first was a parallel inclined shear crack above the critical shear crack, and the second was an inclined shear crack on the right beam side. The cracks were attracted by weak ITZs around aggregates (Fig. 5). No cracks were noticed in the concrete cover.

3. Formulation of discrete element method (DEM) for concrete

3.1. DEM for cohesive-frictional materials

The 3D open-source DEM software YADE [56,57], which permits overlap between two contacted bodies (soft-particle model), was used to run DEM simulations. Particles in a DEM interact with one another during translational and rotational motions using Newton's second law of motion and an explicit time-stepping approach [63]. Because DEM takes into account inertial forces, it is a dynamic technique. The model predicts a cohesive bond at the grain contact with a brittle failure below the critical normal tensile force. Shear cohesion failure under typical compression results in contact stick and slip, which are governed by the Coulomb friction law. Regularization is not required for DEM that does not use partial differential equations, so using this approach yields a discrete equation system that is well-posed. Fig. 6 shows the mechanical response of DEM for particles. The following is a list of DEM formulas:

$$\vec{F}_n = K_n U \vec{N} \tag{1}$$

$$\vec{F}_s = \vec{F}_{s,prev} + K_s \Delta \vec{X}_s, \tag{2}$$

$$K_n = E_c \frac{2R_A R_B}{R_A + R_B} \quad \text{and} \quad K_s = v_c E_c \frac{2R_A R_B}{R_A + R_B} \tag{3}$$

$$\|\vec{F}_s\| - F_{max}^s - \|\vec{F}_n\| \times \tan\mu_c \leq 0 \quad \text{(before contact breakage)}, \tag{4}$$
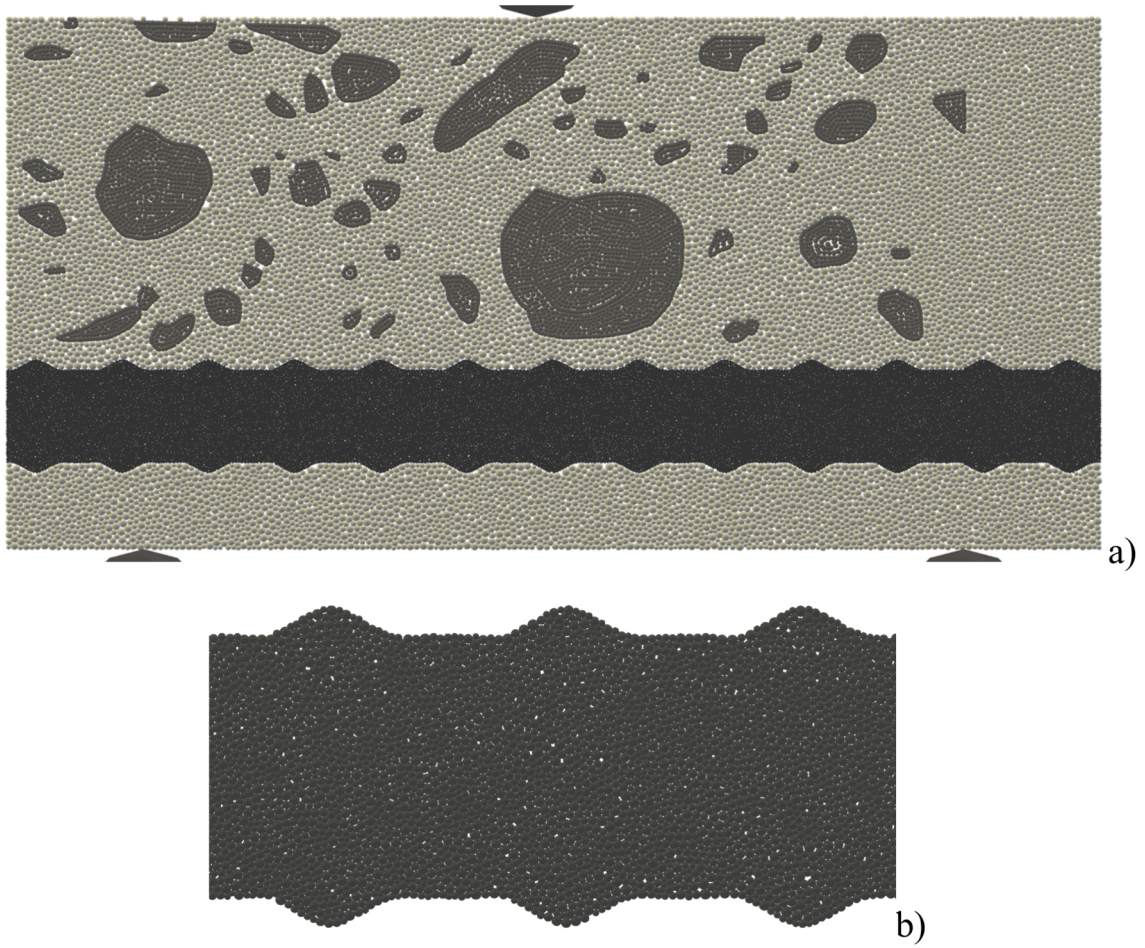
Fig. 7. 2D model of RC beam 40 mm × 80 mm: a) entire beam based on Fig.5 and b) part of steel ribbed bar (light grey color denotes mortar, dark grey color denotes aggregate and black color corresponds to steel ribbed).

$$\| \overrightarrow{F}_s \| - \| \overrightarrow{F}_n \| \times \tan\mu_c \ \leq 0 \quad \text{(after contact breakage)}, \tag{5}$$

$$F^s_{max} = CR^2 \quad \text{and} \quad F^n_{min} = TR^2 \tag{6}$$

$$\overrightarrow{F}^k_{damp} = \overrightarrow{F}^k - \alpha_d \bullet \text{sgn}\left(\overrightarrow{v}^k_p \right) \overrightarrow{F}^k \tag{7}$$

where $\overrightarrow{F}$ – the normal contact force, U – the overlap between discrete elements, $\overrightarrow{N}$ – the unit normal vector at the contact point, $\overrightarrow{F}_s$ – the tangential contact force, $\overrightarrow{F}_{s,prev}$ – the tangential contact force in the previous iteration, $\overrightarrow{X}_s$ – the relative tangential displacement increment, K_n – the normal contact stiffness, K_s – the tangential contact stiffness, E_c – the elastic modulus of the particle contact, v_c – the Poisson's ratio of particle contact, R – the particle radius, R_A and R_B – the contacting particle radii, μ_c – the Coulomb inter-particle friction angle, F^s_{max} – the critical cohesive contact force, F^n_{min} – the minimum tensile force, C – the cohesion at the contact (maximum shear stress at zero pressure), and T – the tensile strength of the contact, $\overrightarrow{F}^k_{damp}$ – the dampened contact force, $\overrightarrow{F}^k$ and $\overrightarrow{v}^k_p$ – the kth components of the residual force and translational particle velocity v_p, and α_d – the positive damping coefficient smaller than 1 (sgn(•) that returns the sign of the kth component of velocity).

The following material constants are required for DEM simulations: E_c, v_c, μ_c, C, and T. Non-viscous damping was assumed [64] (Eq.7) in simulations to speed up convergence. Additionally necessary are the parameters R, ρ (mass density), and α_d. To accurately replicate the distribution of shear and tensile cracks, the relationship between the uniaxial compressive and tensile strength, and the failure mode of specimens (brittle or quasi-brittle, shear or tensile), the particle contact ratio C/T must be carefully considered [65]. As the C/T ratio grows, a more brittle and tensile failure mode dominates, and more tensile cracks appear.

Typically, the material constants are determined by running several DEM simulations and comparing the outcomes to experimental
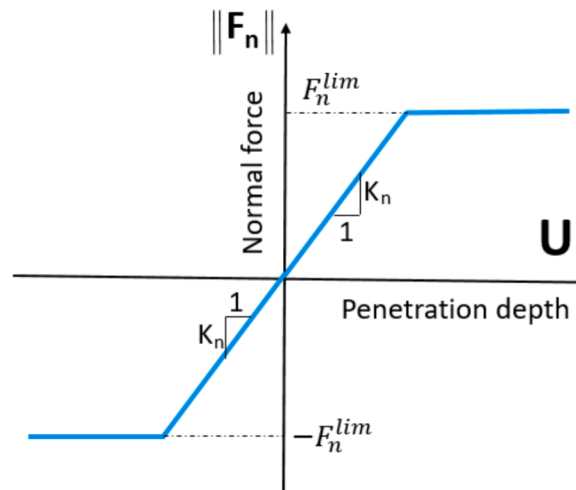
Fig. 8. Normal contact model in DEM for particles imitating steel bar.

Table 1
Main DEM parameters for different phases assumed in simulations.

Material parameters	mortar	ITZs around aggregates	steel ribbed bar	ITZ between mortar and steel bar
T [MPa]	22.5	15.75 (70 % of mortar)	300	15.75 (70 % of mortar)
C [MPa]	22.5	15.75 (70 % of mortar)	300	15.75 (70 of mortar)
E_c [GPa]	11.2	7.84 (70 % of mortar)	67.2	7.84 (70 % of mortar)
v_c [-]	0.2	0.2	0.3	0.2
μ_c [∘]	18	18	0	18

data from simple tests, such as uniaxial compression [5,29], triaxial compression, and simple shear. In simulations, we assumed material constants based on a simple laboratory test (as uniaxial compression) on concrete specimens due to a lack of detailed information concerning the strength properties of mortars with different initial porosity. The damping factor was set to $\alpha_d = 0.08$ consistently. The loading velocity v for this value has no impact on the outcomes [29]. Damage is assumed if a cohesive joint (Eq.6) between two spheres disappears after passing a critical threshold. The cohesion does not exist if any connections between spheres are re-established after failure (Eq.5). Material softening is not taken into account by the DEM model. Due to the potential for particle overlap in DEM, any micro-porosity may be reached. The model was successfully used by the authors to represent the behavior of numerous engineering materials having a particulate structure, such as granulates [66–69], concretes [5–7,32–34], and rocks [65,70,71]. This was accomplished by taking into account shear localization and fracture. Grain fragmentation is not taken into consideration by the current DEM model. This issue can be taken into account in DEM simulations although there will be a significant increase in computing time. Due to calculating time constraints, DEM cannot be recommended as a numerical tool for large concrete or reinforced concrete elements. There are, some up-scaling techniques used with DEMs, such as mass/density/gravity scaling or grain up-scaling (precise scaling of grains and coarse-graining). However, when strain localization occurs in concrete, those up-scaling techniques fail. Since the size of the localized strain cannot be scaled because it depends on the initial and boundary conditions of the entire system, scaling is not feasible. It must be noted that enhanced continuum models enhanced by a characteristic length of mesostructure (related to the aggregate size) require very fine meshes to obtain mesh-independent results in the case of strain localization. For example, when using non-local models, the element size should not be greater than the double characteristic length ([3,72,73]).

4. DEM input data

The experiment's 40 mm × 80 mm geometry was replicated in the 2D numerical beam with a reinforcing steel ribbed bar (Fig. 7). To deform the beam assembly, a constant vertical velocity of $v = 5$ mm/s was applied at the position of the vertical force F using a steel loading cylinder. This vertical velocity was small enough to consider the test as quasi-static. The mean inertial number I which quantifies the significance of dynamic effects was kept below 10^{-4} which always corresponds to a quasi-static regime [74]. Concrete was modeled as a three-phase material made up of mortar, aggregate, and ITZs. Macro-pores were not taken into account. The
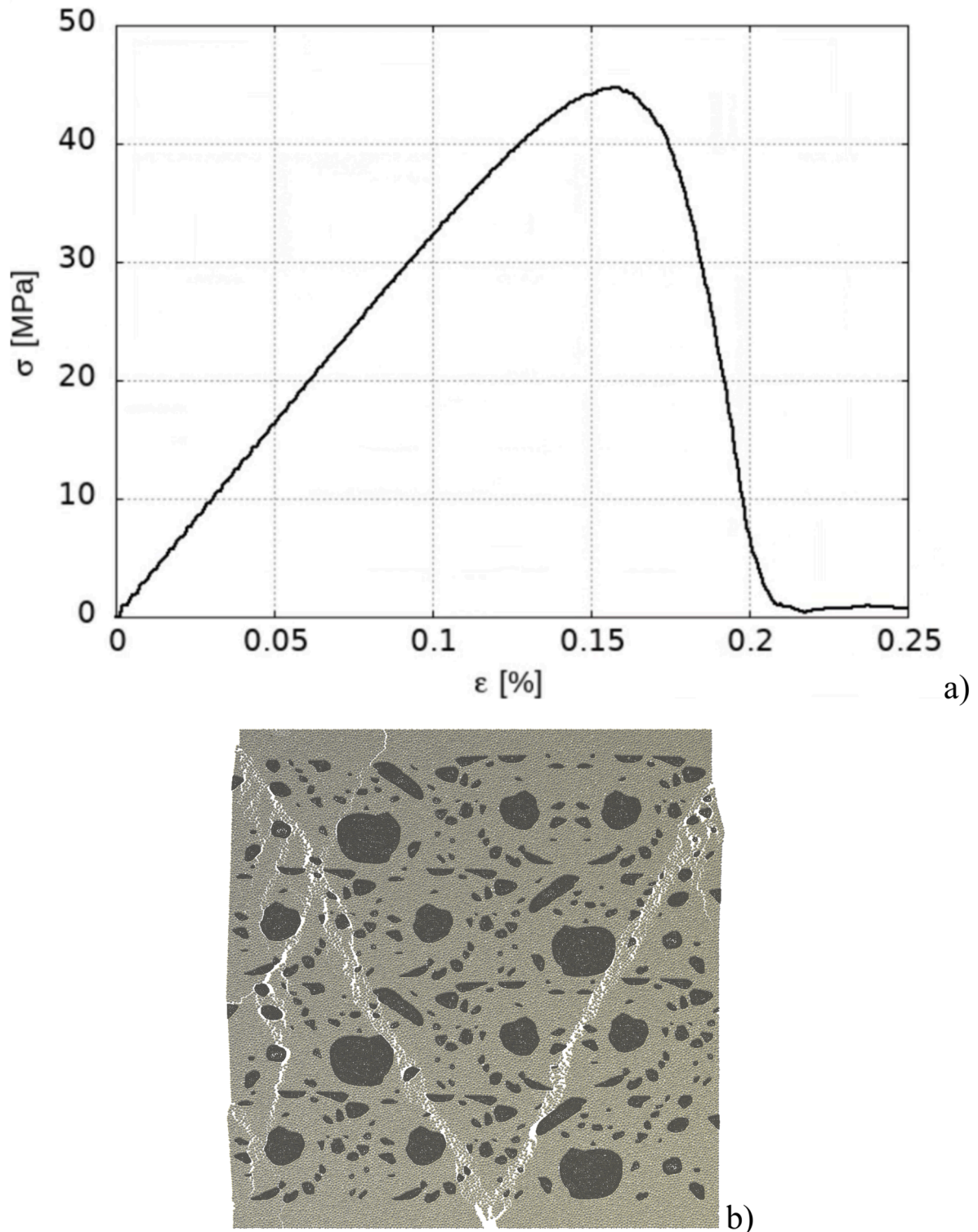
Fig. 9. DEM results for concrete specimen under 2D uniaxial compression: a) stress–strain curve $\sigma = f(\varepsilon)$ and b) failure mode.

aggregate range (with ITZs) was between 1 mm and 16 mm. Clusters of 0.4 mm diameter spheres were used as the aggregate particles in order to faithfully reproduce their shape. Based on micro-CT scans, the dimensions, configuration, and placement of each aggregate were directly retrieved from the actual specimen (Fig. 5). Spheres with diameters ranging from 0.35 mm to 1.0 mm were used to
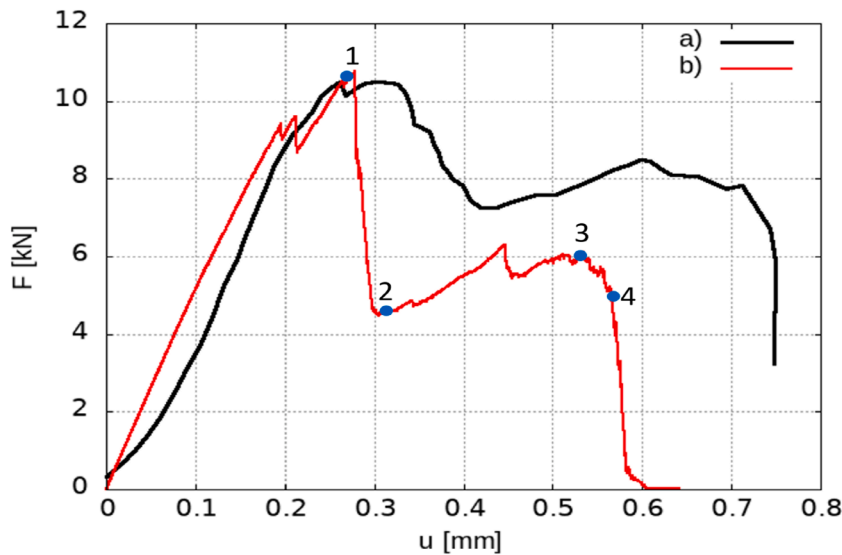
Fig. 10. Force-deflection curve F = f(u): a) experiment [51] and b) DEM calculation (with some characteristic points '1'-'4').

simulate the mortar in the beam. The effect of d_{min} on the stress–strain curve in DEM simulations is negligible if d_{min} is small enough, i.e. $d_{min} \leq 0.25$–0.50 mm [36]. The beam's initial porosity of $p = 2.7$ % matched the experimental value (Section 2).

The geometry of the steel ribbed bar was replicated in 2D simulations. Densely packed spherical components with diameters varying between 0.15 mm and 0.35 mm were used to construct the steel bar with rib heights of 0.70 mm. The bar height was equal to its diameter. The normal bilinear contact model in DEM for particles imitating a steel bar is shown in Fig. 8. It was calibrated to match the global elastic modulus of steel of $E = 200$ GPa and steel yielding of $f_y = 650$ MPa during uniaxial tension (Section 2). The bar pullout failure mode may occur in the calculations since the mortar particles were not fixed to the bar. ITZs around aggregates and between steel bar and mortar particles were modeled as weaker contacts with no physical width explicitly defined [5,34–36]. The ratio $E_{c,ITZ}/E_{c,cm} = 0.70$ was chosen based on the nanoindentation experiments [6,76]. The remaining two ratios, C_{ITZ}/C_{cm} and T_{ITZ}/T_{cm}, were also assumed to be equal to 0.70 as in earlier DEM simulations [5,34,35] due to a lack of experimental data for mortars of different initial porosity. Based on triaxial compression tests with clumped granulates, the inter-particle friction angle of $\mu_c = 18°$ was postulated [77]. The same ratios of $E_{c,bond}/E_{c,cm} = 0.70$, $C_{bond}/C_{cm} = 0.70$, and $T_{bond}/T_{cm} = 0.70$ were also assumed in ITZ between the ribbed bar and mortar again due to a lack of experimental pull-out data for with mortars of different initial porosity. A total of 32'000 DEM elements were used, with 14'000 elements modeling steel bar, 12,500 elements modeling mortar, and 5'500 elements modeling aggregate (Fig. 8). The width of the beam cross-section was equal to the grains' diameter. The aggregates in amount 4 in the concrete cover of a thickness of 7 mm were disregarded since there were no visible cracks beneath the bar (Fig. 5). About five days were needed to finish the calculations on a computer with a 3.30 GHz CPU. The computational cost of the simulation was relatively high because the existing DEM model was parallelized on threads only but not in a distributed mode (on cluster computer nodes). In Table 1, the material parameters chosen in DEM computations are listed (with the C/T ratio equal to 1). The parameter F_n^{lim} (Fig. 7) was taken as $|F_N^{lim}| = 18.15 \times 10^6$ kN.

The DEM material parameters for concrete (Tab.1) were validated with the aid of 2D uniaxial compression tests on rectangular concrete specimens measuring 10×10 cm^2 (Fig. 9) without performing micro-CT images. The calculated compressive strength, modulus of elasticity, and Poisson's ratio were compared with the experimental values. The tensile fracture energy was not calibrated since the DEM model does not include softening. The concrete mesostructure in the specimen under compression was similar to that in the beam (the segment of the beam mesostructure was a few times replicated within the concrete specimen). The initial porosity was also the same $p = 2.7$ %. The same calibration procedure was proved to be sufficient in earlier 2D DEM simulations for concrete by assuming the artificial mesostructure [5–7,34,36]. The predicted compressive strength of concrete was approximately $f_c = 46$ MPa (Fig. 9a), slightly lower than the experimental one of $f_c = 49.75$ MPa (Section 2). The predicted elastic modulus was $E = 32$ GPa (Fig. 9a), also slightly lower than the experimental value of $E = 34.8$ GPa (Section 2). The predictive Poisson's ratio was $\nu = 0.21$ as in the laboratory test (Section 2). Inside the specimen three evident macro-cracks were numerically obtained: two inclined and one almost vertical (Fig. 9b).

5. DEM results

### 5.1. Force-deflection curve

For the vertical beam mid-plane passing the ribbed bar (Fig. 5), DEM computations were performed. Fig. 10 contrasts the experimental evolution with the expected evolution $F = f(u)$. Despite some differences, there is reasonable agreement regarding the
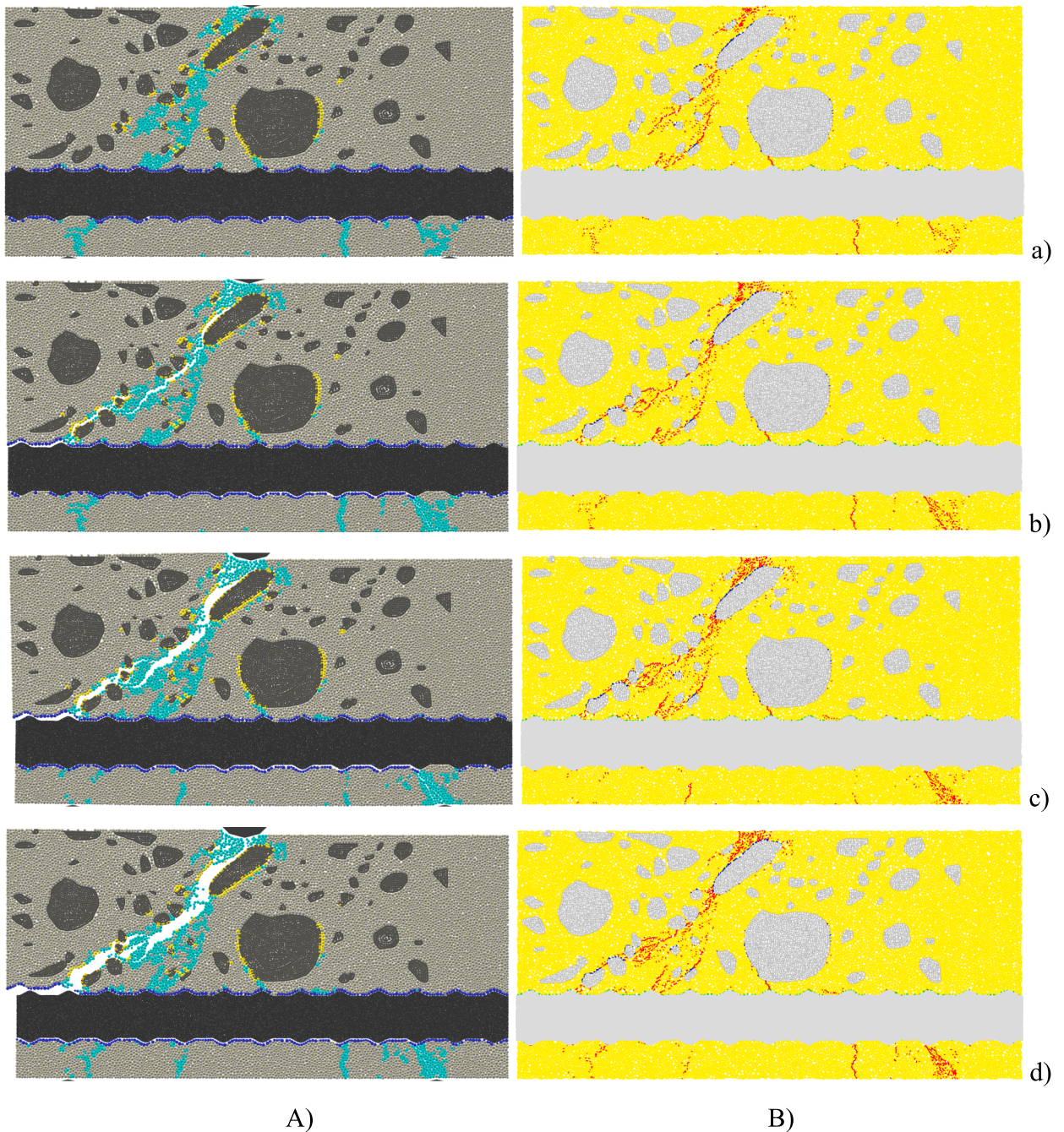
Fig. 11. Deformed A) and non-deformed beam B) with broken contacts in three-point bending during deflection u (Fig.10): a) $u = 0.277$ mm (before load peak, point '1' in Fig.10), b) $u = 0.302$ mm (before re-hardening phase, point '2' in Fig.10), c) $u = 0.538$ mm (after re-hardening phase, point '3' in Fig.10) and d) $u = 0.570$ mm (failure phase, point '4' in Fig.10) (colors denote in broken contacts: magenta – mortar, yellow – ITZs around aggregates, and blue – ITZ along steel bar in Fig.11A and red – beam in Fig.11B).

force–deflection curve's shape. The experimental data ($F_{max} = 10.5$ kN and $u = 0.30$ mm) and the calculated maximum vertical force ($F_{max} = 10.5$ kN) and deflection corresponding to F_{max} ($u = 0.277$ mm) were comparable. Initially, there was also a similar stiffness. The highest value of the vertical force was followed by a decline in the maximum vertical force. In DEM simulations, this drop, however, was too strong and too fast. The simulation then went through the same re-hardening phase as the experiment did. In DEM analyses, the beam failure occurred too quickly (deflection $u = 0.58$ mm versus $u = 0.74$ mm in the experiment). The 3D simulations with a larger amount of discrete elements in the mortar should be used to decrease the beam brittleness after reaching the maximum force F_{max}, based on our earlier DEM calculations for a concrete beam [5] which indicated the concrete brittleness growth in 3D
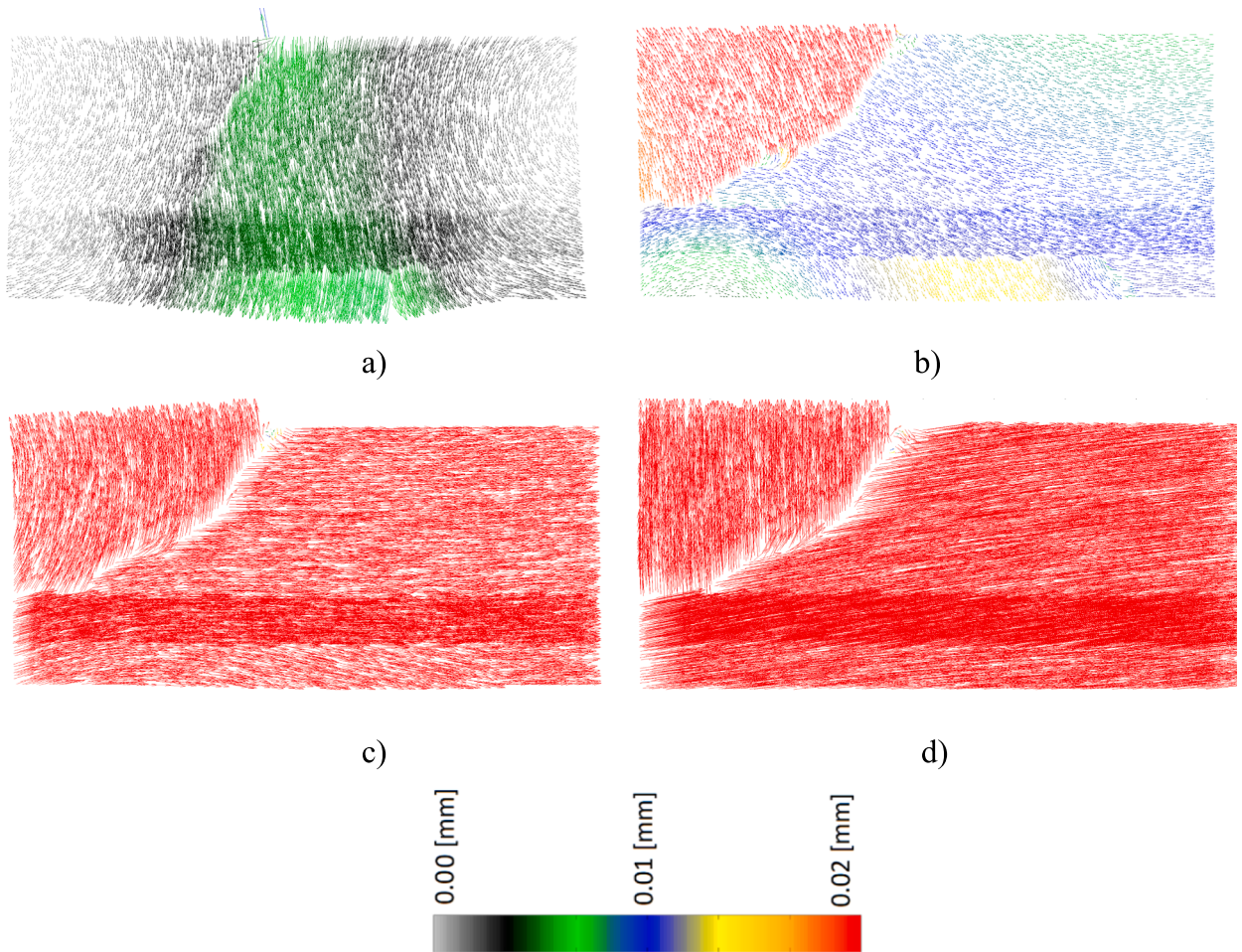
Fig. 12. Evolution of displacement vectors of discrete elements during beam deflection u: a) $u = 0.277$ mm (before load peak), b) $u = 0.302$ mm (before re-hardening phase), c) $u = 0.538$ mm (after re-hardening phase) and d) $u = u = 0.570$ mm (damage phase) (displacement scale is attached).

simulations compared to 2D ones.

5.2. Fracture process

The crack progression in the deformed and non-deformed beam based on computed displacements and broken connections is shown Fig.11. Initially, many microcracks emerged in ITZs surrounding aggregates and along the ribbed bar up to the maximum vertical force for $u = 0.28$ mm (point '1' in Fig. 10), a few bending cracks appeared at the bottom of the beam, and a few cracks appeared below the vertical force and at the supports owing to compression (Fig. 11a). Between the vertical force and left support, a branching inclined shear crack (similar to that in the experiment (Fig. 3) also appeared (Fig. 11a). The branched shear crack broke into a primary and secondary shear crack at the end of the softening range (point '2' in Fig.10), as seen in Fig. 11b. Later on (points '3' and '4' in Fig. 10), the primary shear crack widened into a critical one (Figs. 11c and 11d). The calculated mean crack inclination to the horizontal (about 45°) was similar to the experiment. The numerical crack propagated under two aggregate particles in the beam mid-part and above two aggregate particles at the beam bottom in contrast to the experiment. Precise placement of aggregates in calculations had a crucial effect on the crack geometry due to the presence of weak ITZs that attracted the diagonal shear crack. The estimated failure mechanism was similar to the experimental one (failure in shear due to a diagonal shear crack) (Fig. 5). However, any secondary shear cracks of Fig. 5 were numerically obtained.

Fig. 12 displays the displacement vector maps of individual discrete elements during beam deflection. The vectors were initially multiplied by a factor of 20 and progressively decreased to a factor of 3 for the final steps. The plot's colors represent computed displacement, with the red color designating the biggest displacement (about 0.02 mm). At first, displacements of vertical elements took place below the vertical force (Fig.12a). Later, the right beam component experienced horizontal movement of elements, whereas the left beam part experienced both vertical (upward) and horizontal movements as a result of the development of a primary inclined shear crack (Figs.12b and 12c). The left beam part finally separated from the reinforcement bar (Fig.12d).
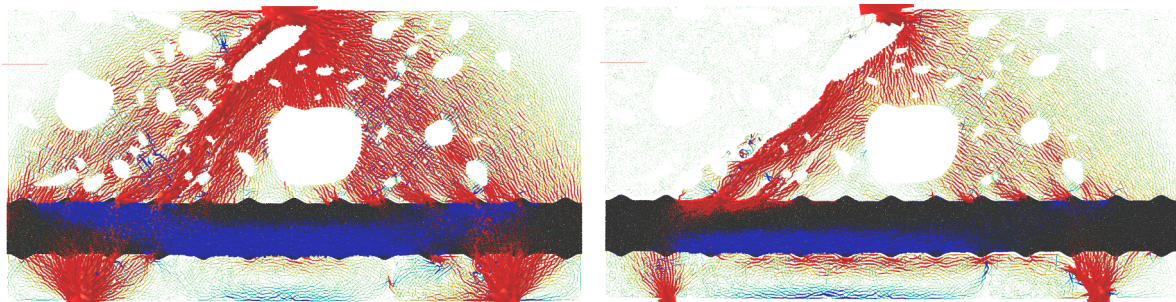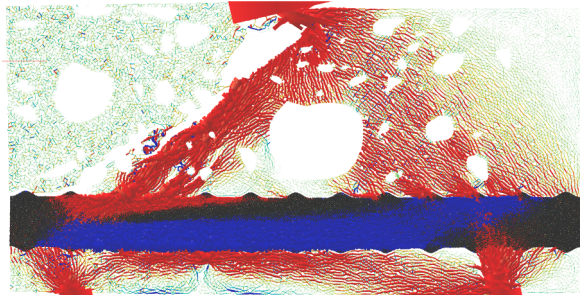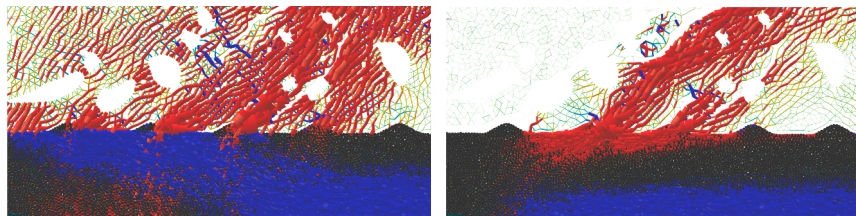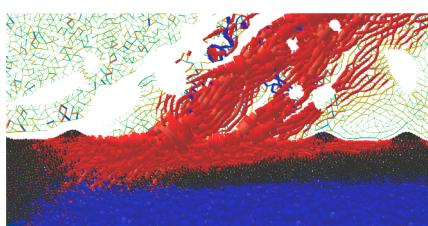
Fig. 13. Evolution of normal contact forces in RC beam (A) and zoom on bar ribs (B) during three-point bending for deflection *u*: a) $u = 0.277$ mm (before load peak), b) $u = 0.302$ mm (before re-hardening phase), c) $u = 0.538$ mm (after re-hardening phase) and d) $u = 0.570$ mm (damage phase) (red color denotes large compressive forces, and blue color denotes large tensile forces – larger than the average ones).

5.3. Contact forces

Figures 13 and 14 show the development of normal and tangential contact forces between discrete elements. The red and blue colors indicate forces higher than their mean compressive/tensile value. The region under the vertical force and two supports initially experienced strong inclined compressive normal forces (Fig.13a). At both beam sides, they were supported by four bar ribs. Strong
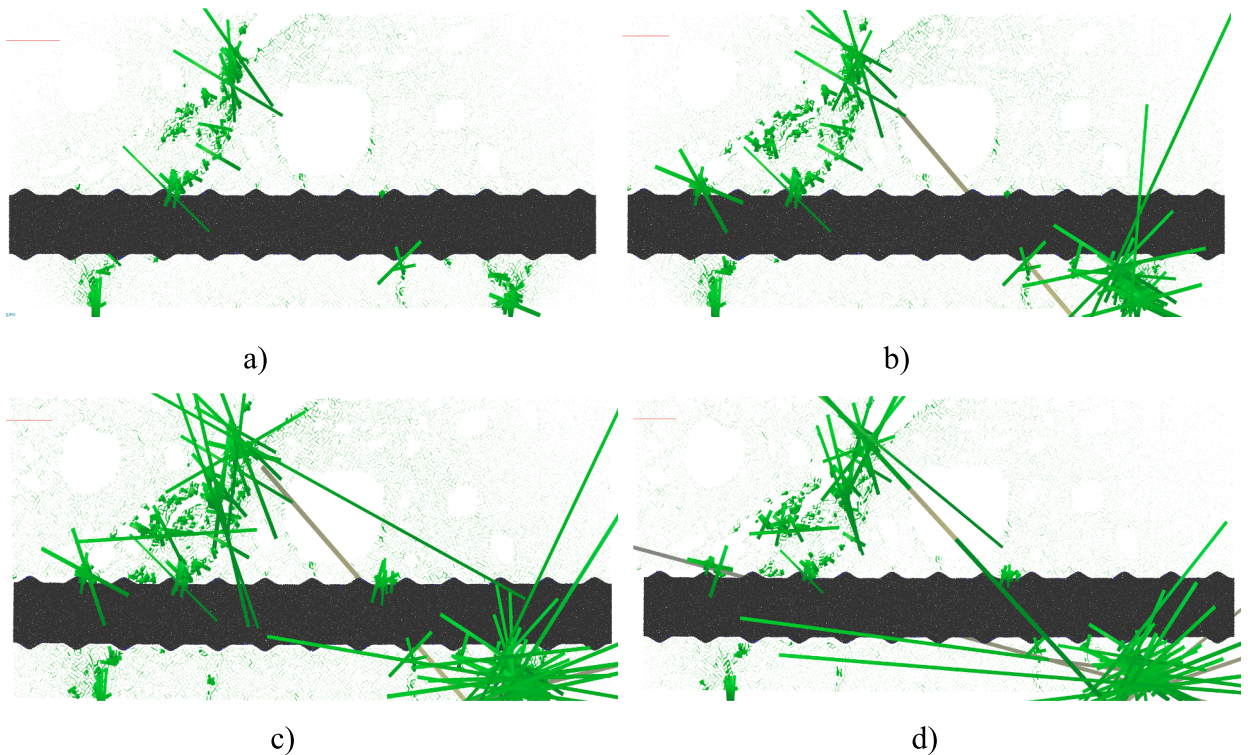
Fig. 14. Evolution of larger tangential contact forces during three-point bending for deflection u: a) $u = 0.277$ mm (before load peak), b) $u = 0.302$ mm (before re-hardening phase), c) $u = 0.538$ mm (after re-hardening phase) and d) $u = 0.570$ mm (damage phase).
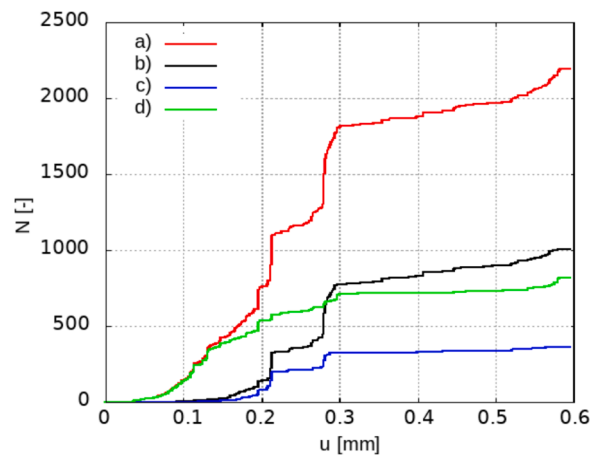

Fig. 15. Evolution of broken contacts N during beam deflection u: a) entire beam, b) mortar, c) ITZs around aggregates and d) ITZ along steel bar.

tensile forces were also seen in the bending steel bar at the same time. Then, the horizontal compressive normal contact forces began to concentrate along the bar rib and the inclined compressive normal forces started to concentrate in the left beam part (supported by only two bar ribs) (Fig.13b). Thus, significant redistribution of the contact forces was due to the creation of the inclined shear crack. During the re-hardening phase, all compressive contact forces strengthened (Fig.13Ac). The compressive strut in the left beam region temporarily wedged between the bar ribs, which led to the global re-hardening (the shear crack was arrested). Later, the contact forces softened (Fig.13Ad). High tangential contact forces (higher than the mean value) mainly occurred in the critical diagonal shear crack and at the beam supports (Fig.14).

In Fig.15, the development of broken contacts during bending is seen. The total number of broken contacts at the end of the numerical test (curve 'a' in Fig.15) was 2'200 (around 2.8 % of all initial contacts in the RC beam). Up at the maximum vertical force ($u = 0$–0.28 mm) and in the softening region ($u = 0.28$–0.30 mm), the highest number of cracks was created. Long before the peak (curve 'd'
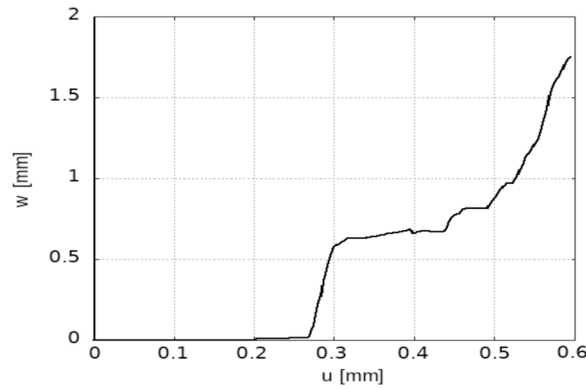
Fig. 16. Evolution of critical crack width w during three-point bending versus deflection u.

in Fig.15), the first indications of micro-cracking were seen in ITZ along the steel bar for $u = 0.018$ mm. Micro-cracks then developed in the mortar and ITZs surrounding the aggregates (see curves 'b' and 'c' in Fig.15). The mortar and ITZ along the bar had the greatest microcracking just before the peak force for $u = 0.28$ mm. A few contacts in the mortar were broken throughout the re-hardening phase and the beam damage phase. The mortar, ITZs along the bar, and ITZs near aggregates had sequentially the highest contact breakage rate during beam loading.

The development of the width of the inclined critical shear crack at its midpoint is depicted in Fig.16. The calculated crack widths w were equal to 0.19 mm before reaching the maximum force (F_{max}), 0.67 mm in the re-hardening phase mid-point, and 1.35 mm in the failure phase for $u = 0.55$ mm. They were slightly greater than the experimental ones (0.16 mm, 0.50 mm, and 1.25 mm). The beam experienced the largest rise in the crack width increment in both the softening phases ($u = 0.28$–0.30 mm and $u = 0.55$–0.60 mm) (Fig.16). A re-hardening process ($u = 0.30$–0.45 mm) did not cause the crack's width to increase since the shear crack was arrested in the bar ribs (Fig.13).

5.4. Stresses in concrete along bar

Next, along the steel bar, starting from the height just above the ribs, the normal and shear stresses in concrete were calculated. This region's height was chosen to be equal to $d_{50} = 2$ mm. The Cauchy-Weber formula, a standard method for calculating stresses in discrete mechanics, was used [75]

$$\sigma_{ij} = \frac{1}{A} \sum\nolimits_{c=1}^{N_c} f_i^c l_j^c, \tag{8}$$

where A is the REV area, N_c is the number of contacts inside REV, f_i^c is the contact force between two elements in the i-direction, and l_j^c is the distance between two centers of elements in contact in the j-direction.

Fig. 17 shows the normal and shear stresses along the steel bar length L at various deflections u (u_x denotes the horizontal coordinate against the beam's vertical centerline). Because there were ribs, the wall stress distributions were not uniform along the bar. Due to the extremely high wall roughness of the steel bar, the shear stresses were similar to the normal ones (the wall friction angle was roughly 45°). Before the fracture process, the stresses along the bar were almost symmetric against the vertical axis (Fig.17A). Afterward, they slightly increased on the left beam side due to the appearance of the shear crack (Figs.17B and C). As the shear crack developed, the stresses continued to be non-symmetric and higher on the left beam side (Figs.17C–E). The maximum shear stress reached approximately 20 MPa. During damage for $u = 0.570$ mm (Fig.17F), the stresses dropped drastically.

The evolution of the wall shear stress τ_w versus the horizontal displacement u_s in concrete along the steel bar (slip) for 3 points in the left beam region: $u_x = -20$ mm (on the right of the diagonal shear crack), $u_x = -30$ mm (under the shear crack) and $u_x = -38$ mm (on the left of the shear crack) is shown in Fig.18. The shape of the bond-slip curve $\tau_w = f(u_s)$ during bending was different in all three points after reaching the maximum value of about 9 MPa in contrast to unique bond-slip laws assumed between the mortar and steel bar.

5.5. Effect of material parameters in ITZ

It was investigated how material parameters in ITZ between concrete and a steel bar affected the force–deflection curve and failure mode (Figs.19 and 20). About the mortar characteristics, the basic values of E_c, C, and T in ITZ (Tab.1) were reduced by 15 % and 60 %, respectively.

There were no observable variations in the maximum vertical force (Fig.19). The rate of softening was likewise comparable. However, the ITZ weakening strongly shortened the length of the re-hardening zone whereas the ITZ strengthening enlarged the re-hardening zone on the force–deflection diagram (Fig.19).

The failure modes in Fig.20 demonstrate how the they were impacted by the material characteristics in ITZ between concrete and a steel bar. When E_c, C, and T values in ITZ (Tab.1) were reduced by 60 % (Fig.20a), there was a steeper critical diagonal shear fracture.
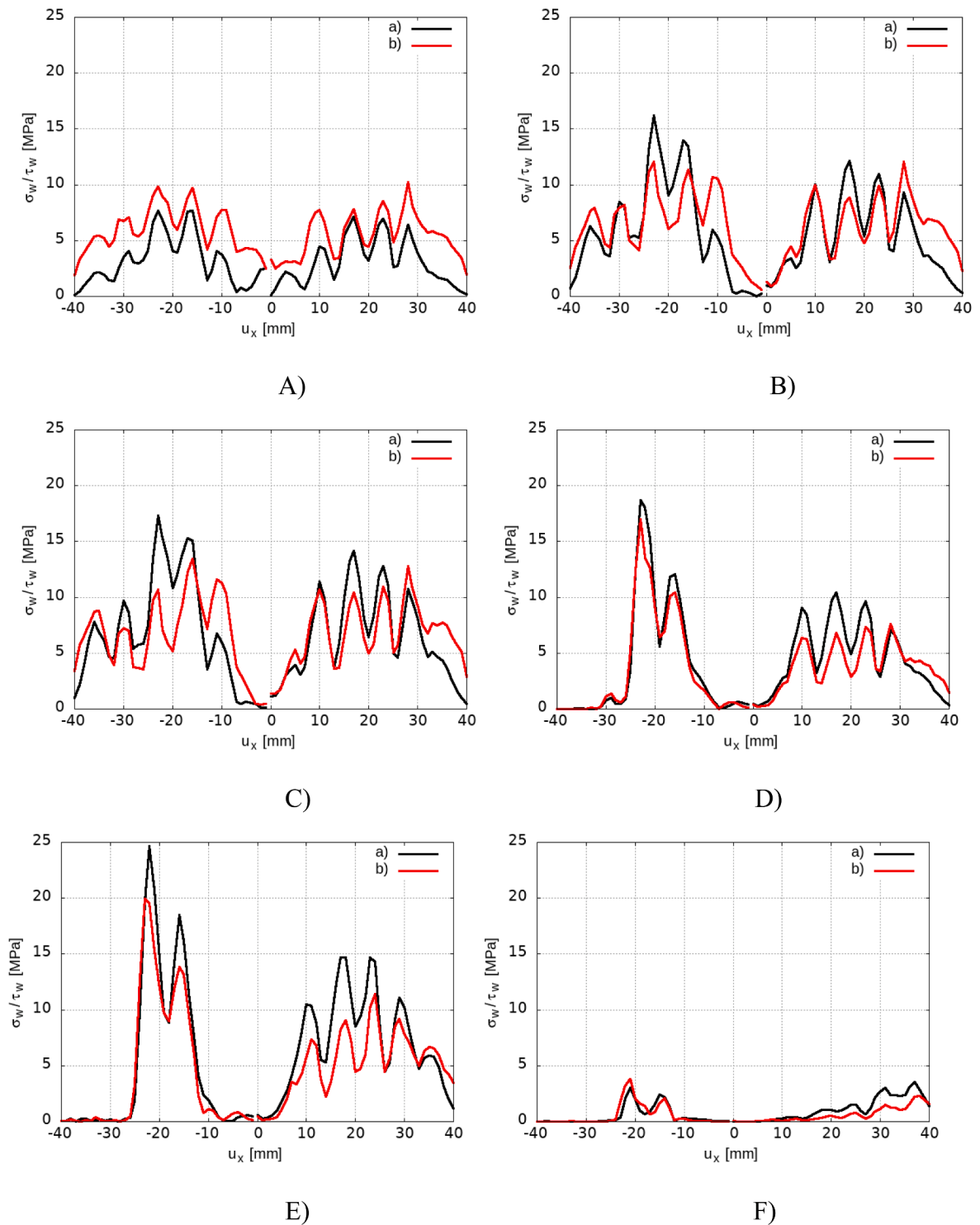
Fig. 17. Normal σ_w (a) and shear wall stresses τ_w (b) along steel bar length L during beam deflection u: A) $u = 0.176$ mm (before shear crack), B) $u = 0.227$ mm (after first crack), C) $u = 0.277$ mm (before load peak), D) $u = 0.302$ mm (before re-hardening phase), E) $u = 0.538$ mm (after re-hardening phase) and F) $u = 0.570$ mm (damage) (u_x denotes horizontal coordinate against vertical centerline).
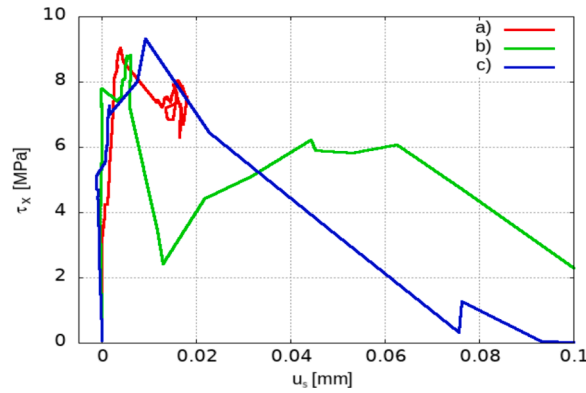
Fig. 18. Evolution between wall shear stress τ_w and horizontal displacement u_s for three points along steel bar: a) u_x = -20 mm, b) u_x = -30 mm and c) u_x = -38 mm (u_x denotes horizontal coordinate against vertical centerline).
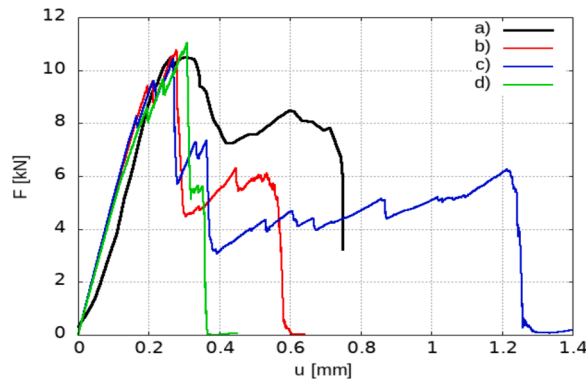
Fig. 19. Force-deflection curve F = f(u): a) experiment [51] and b-d) DEM results for different parameters of ITZ between steel bar and mortar: b) $E_{c,bond}/E_{c,cm}$ = 0.70, C_{bond}/C_{cm} = 0.70 and T_{bond}/T_{cm} = 0.70, c) $E_{c,bond}/E_{c,cm}$ = 0.85, C_{bond}/C_{cm} = 0.85 and T_{bond}/T_{cm} = 0.85 and d) $E_{c,bond}/E_{c,cm}$ = 0.40, C_{bond}/C_{cm} = 0.40 and T_{bond}/T_{cm} = 0.40.

Values of E_c, C, and T in ITZ (Tab.1) less by 15 % resulted in more secondary shear cracks (Fig.20b).

5.6. Effect of concrete mesostructure

Finally, an investigation was conducted into how the various concrete mesostructures affected the crack pattern (Fig.21). The artificial concrete mesostructure was identical to the original one, but it was shifted horizontally by a different magnitude. The failure modes show that the postulated mesostructure had a significant impact on the crack pattern (Fig.21). When comparing the artificial mesostructure beam to the actual mesostructure beam, the critical shear crack had a greater inclination towards the horizontal (70° versus 45°). The secondary crack pattern also had a distinct appearance. On the left side of the critical shear crack in the beam of Fig.21a, there was another secondary shear crack. In the beam of Fig.21b, a second secondary shear fracture occurred on the opposite side of the critical shear crack.

6. Summary and conclusions

The classical particle discrete element technique (DEM) was used in this study to predict the behavior of an over-reinforced concrete beam with one steel ribbed bar and without vertical reinforcement under quasi-static 2D conditions. The beam in the experiment failed in shear due to a critical diagonal shear crack. A three-phase concrete description, aggregate, mortar, and interfacial transitional zones (ITZs) around aggregates were used to account for the heterogeneity of the concrete at the mesoscale. In DEM calculations based on a 2D X-ray CT scan, the actual shape and placement of aggregate particles in concrete were taken for granted. In analyses, the shape of the steel ribbed bar was precisely reconstructed. ITZ was also assumed in the mortar along the steel bar. A geometrical interface condition was assumed to exist between the concrete and a steel bar without imposing a bond-slip law (being the outcome of simulations). The experiment and the DEM simulations were compared. The 2D DEM analysis results can lead to the following conclusions:
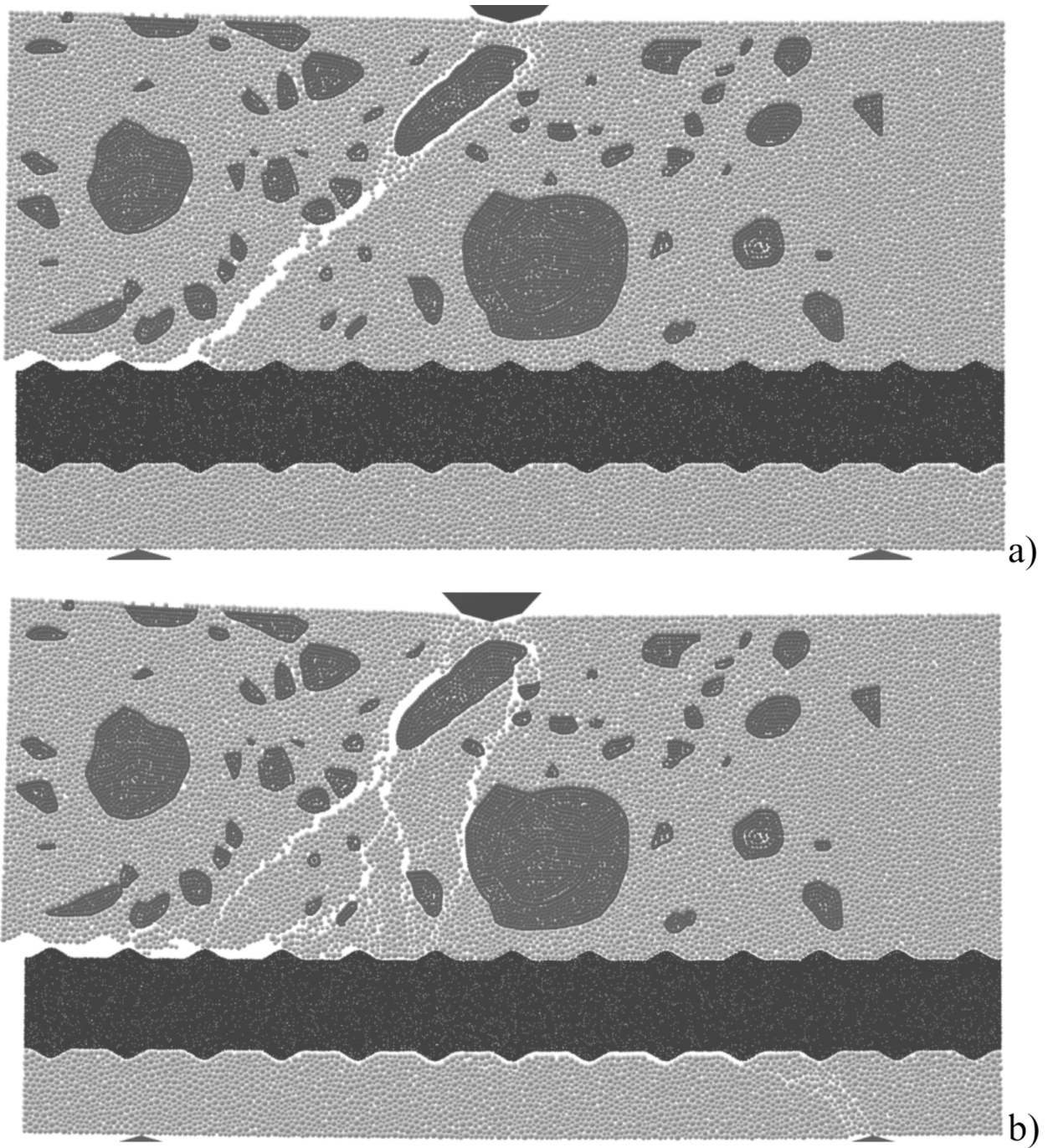
Fig. 20. Deformed beam with broken contacts in three-point bending with two different parameters of ITZ between steel bar and mortar: a) $E_{c,bond}/E_{c,cm} = 0.40$, $C_{bond}/C_{cm} = 0.40$ and $T_{bond}/T_{cm} = 0.40$ and b) $E_{c,bond}/E_{c,cm} = 0.85$, $C_{bond}/C_{cm} = 0.85$ and $T_{bond}/T_{cm} = 0.85$ (colors denote in broken contacts: magenta – mortar, yellow – ITZs around aggregates, and blue – ITZ along steel bar).

– The evolution of the vertical force against the deflection and a critical diagonal shear crack were satisfactorily matched by the DEM calculations to the experiment despite simplified 2D conditions. There existed the following discrepancies: the beam response was too brittle and the experimental secondary shear cracks were not obtained in the simulations. The planned 3D calculations considering macro-pores should improve DEM results regarding the experimental observations. Precise placement of aggregates with surrounding weak ITZs in mesostructure had a primary effect on the critical crack's propagation way. The effect of the different concrete mesostructures on the crack pattern was evident. The crack pattern was also influenced by the properties of ITZ between the mortar and steel bar.
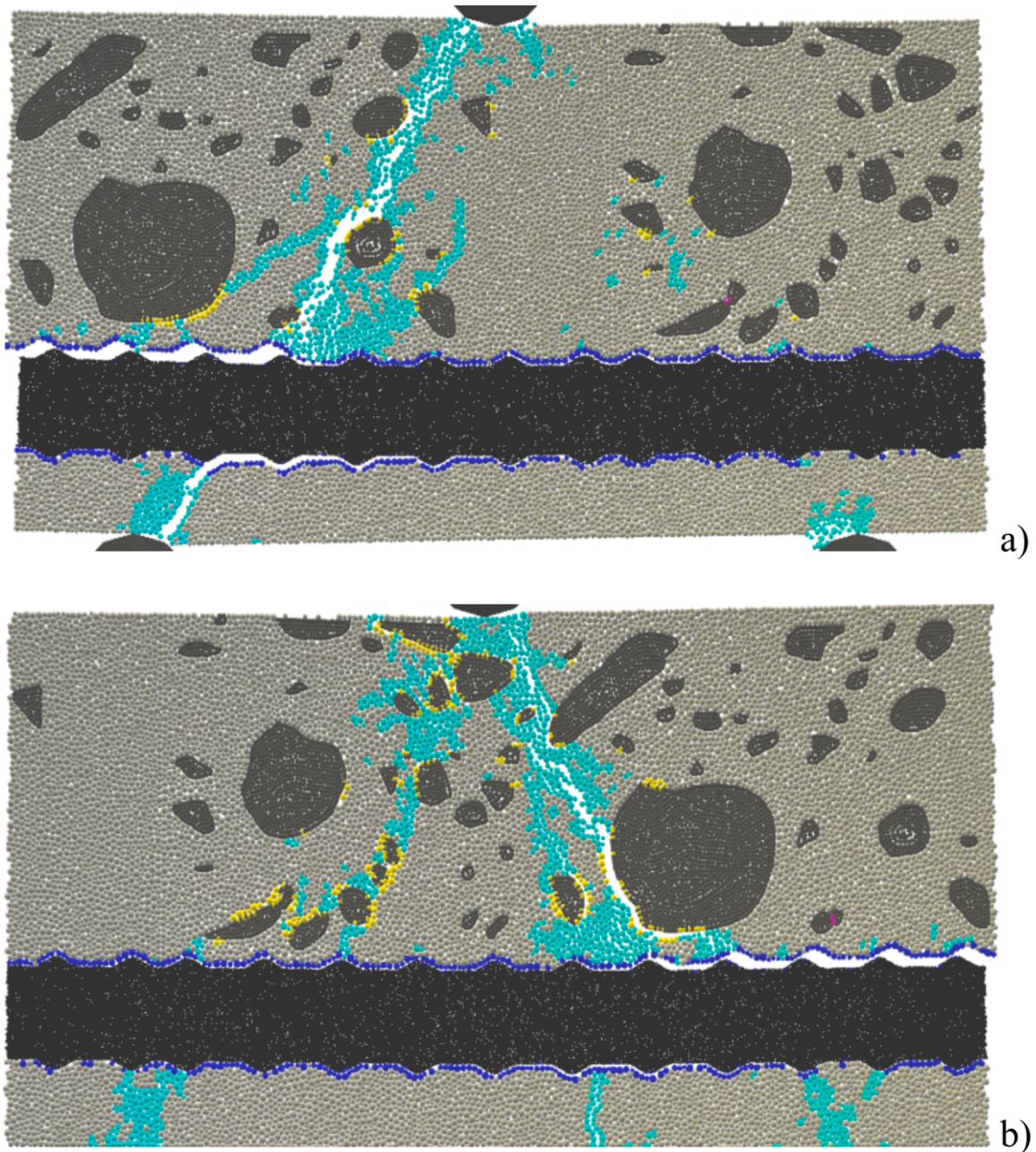
Fig. 21. Deformed beam with broken contacts in three-point bending with two different initial mesostructures a) and b) (colors denote in broken contacts: magenta – mortar, yellow – ITZs around aggregates, and blue – ITZ along steel bar).

– A geometric bond condition depicted the bond between the steel bar and concrete more realistically than a standard bond-slip rule. Along the steel bar, the bond-slip curve's shape changed.
– The mortar, ITZs along the bar, and ITZs adjacent to aggregates had the highest contact breakage rates.
– A temporary critical shear crack's arrest in steel bar ribs led to a global re-hardening phase.
– The weakening of ITZ between the mortar and steel bar shortened the length of the re-hardening region on the force–deflection diagram.

CRediT authorship contribution statement

Michał Nitka: Visualization, Software, Methodology, Investigation, Formal analysis, Conceptualization. **Jacek Tejchman:** Writing – original draft, Supervision, Project administration, Funding acquisition, Conceptualization.

Declaration of competing interest

The authors declare that they have no known competing financial interests or personal relationships that could have appeared to influence the work reported in this paper.

Data availability

Data will be made available on request.

Acknowledgements

References

[1] Carpinteri A, Ingraffea AR. *Fracture mechanics of concrete* (Martinus Nijhoff, ed.). The Netherlands 1984.
[2] Bažant Z, Planas J. Fracture and size effect in concrete and other quasi-brittle materials. Boca Raton: CRC Press LLC; 1997.
[3] Tejchman J, Bobiński J. *Continuous and discontinuous modelling of fracture in concrete using FEM*. Springer, Berlin-Heidelberg (eds. W. Wu and R. I. Borja), 2013.
[4] van Mier JGM. Fracture processes of concrete. CRC Press; 2017.
[5] Nitka M, Tejchman J. A three-dimensional meso scale approach to concrete fracture based on combined DEM with X-ray μCT images. Cem Concr Res 2018;107: 11–29.
[6] Nitka M, Tejchman J. Meso-mechanical modelling of damage in concrete using discrete element method with porous ITZs of defined width around aggregates. Engng Fract Mech 2020;231:107029.
[7] Nitka M, Tejchman J. Comparative DEM calculations of fracture process in concrete considering real angular and artificial spherical aggregates. Engng Fract Mech 2020;239:107309.
[8] Lyu K, Garboczi EJ, She W, Miao C. The effect of rough vs. smooth aggregate surfaces on the characteristics of the interfacial transition zone. Cement and Concrete Composite 1996;99:49–61.
[9] Bentur A, Alexander MG. A review of the work of the rilem tc 159-etc: engineering of the interfacial transition zone in cementitious composites. Mater Struct 2000;33(2):82–7.
[10] Scrivener KL, Crumbie AK, Laugesen P. The interfacial transition zone (ITZ) between cement paste and aggregate in concrete. Interface Sci 2004;12:411–21.
[11] Schwartz LM, Garboczi EJ, Bentz DP. Interfacial transport in porous media: application to DC electrical conductivity of mortars. J Appl Phys 1995;78:5898–908.
[12] Delagrave A, Bigas JP, Olivier J, Marchand J, Pigeon M. Influence of the interfacial zone on the chloride diffusivity of mortars. Adv Cem Based Mater 1997;5: 86–92.
[13] Krzaczek M, Nitka M, Tejchman J. Modelling hydraulic and capillary-driven two-phase fluid flow in unsaturated concretes at the meso-scale with a unique coupled DEM-CFD technique. Int J Numer Anal Methods Geomech 2023;47(1):23–53.
[14] Pichler B, Hellmich C. Upscaling quasi-brittle strength of cement paste and mortar: A multi-scale engineering mechanics model. Cem Concr Res 2011;41: 467–76.
[15] Königsberger M, Hlobil M, Delsaute B, Staquet S, Hellmich C, Pichler B. Hydrate failure in ITZ governs concrete strength: A micro-to-macro validated engineering mechanics model. Cem Concr Res 2018;103:77–94.
[16] Skarżyński L, Tejchman J. Modeling the effect of material composition on the tensile properties of concrete. Understanding the tensile properties of concrete (ed. by Jaap Weerheijm) *Woodhead Publishing Limited* 2013;48:52–97.
[17] Gitman IM, Askes H, Sluys LJ. Coupled-volume multi-scale modelling of quasi-brittle material. European Journal of Mechanics A/Solids 2008;27:302–27.
[18] Skarzynski L, Tejchman J. Calculations of fracture process zones on meso-scale in notched concrete beams subjected to three-point bending. European Journal of Mechanics A/Solids 2010;29(4):746–60.
[19] Benkemoun N, Hautefeuille M, Colliat JB, Ibrahimbegovic A. Failure of heterogeneous materials: 3D meso-scale FE models with embedded discontinuities. Int J Numer Meth Eng 2010;82:1671–88.
[20] Shahbeyk S, Hosseini M, Yaghoobi M. Mesoscale finite element prediction of concrete failure. Comput Mater Sci 2011;50(7):1973–90.
[21] Kim SM, Abu Al-Rub RK. Meso-scale computational modeling of the plastic-damage response of cementitious composites. Cem Concr Res 2011;41:339–58.
[22] Ren W, Yang Z, Sharma R, Zhang C, Withers PJ. Two-dimensional X-ray CT image based meso-scale fracture modelling of concrete. Engng Fract Mech 2015;133: 24–39.
[23] Trawiński W, Bobiński J, Tejchman J. Two-dimensional simulations of concrete at aggregate level with cohesive elements based on X-ray μCT images. Engng Fract Mech 2016;168:201–26.
[24] Trawiński W, Tejchman J, Bobiński J. A three-dimensional meso-scale approach with cohesive elements to concrete fracture based on X-ray μCT images. Engng Fract Mech 2018;189:27–50.
[25] Herrmann HJ, Hansen A, Roux S. Fracture of disordered, elastic lattices in two dimensions. Physical Rev B 1989;39:637–47.
[26] Carol I, López CM, Roa O. Micromechanical analysis of quasi-brittle materials using fracture-based interface elements. Int Journal for Numerical Methods in Engineering 2001;52:193–215.
[27] Hentz S, Daudeville L, Donze FV. Identification and validation of a Discrete Element Model for concrete. Journal of Engineering Mechanics ASCE 2004;130(6): 709–19.
[28] Kozicki J, Tejchman J. Modelling of fracture processes in concrete using a novel lattice model. Granul Matter 2008;10:377–88.
[29] Nitka M, Tejchman J. Modelling of concrete behaviour in uniaxial compression and tension with DEM. Granul Matter 2015;17(1):145–64.
[30] Tordesillas A, Kahagalage S, Ras C, Nitka M, Tejchman J. Coupled evolution of preferential paths for force and damage in the pre-failure regime in disordered and heterogeneous, quasi-brittle granular materials. Front Mater 2020;7:79.
[31] Bolander JE, Eliáš J, Cusatis G, Nagai K. Discrete mechanical models of concrete fracture. Eng Fract Mech 2021;257(4):108030.
[32] Dupray F, Malecot Y, Daudeville L, Buzaud EA. Mesoscopic model for the behaviour of concrete under high confinement. Int J Numer Anal Methods Geomech 2009;33:1407–23.
[33] Groh U, Konietzki H, Walter K, et al. Damage simulation of brittle heterogeneous materials at the grain size level. Theor Appl Fract Mech 2011;55:31–8.
[34] Skarzynski L, Nitka M, Tejchman J. Modelling of concrete fracture at aggregate level using FEM and DEM based on x-ray μCT images of internal structure. Engng Fract Mech 2015;10(147):13–35.
[35] Suchorzewski J, Tejchman J, Nitka M. Experimental and numerical investigations of concrete behaviour at meso-level during quasi-static splitting tension. Theor Appl Fract Mech 2018;96:720–39.
[36] Suchorzewski J, Tejchman J, Nitka M. DEM simulations of fracture in concrete under uniaxial compression based on its real internal structure. Int J Damage Mechanics 2018;27(4):578–607.
[37] Lilliu G, van Mier JGM. 3D lattice type fracture model for concrete. Engng Fract Mech 2003;70:927–41.

[38] Kawai T. New discrete models and their application to seismic response analysis of structures. Nucl Eng Des 1978;48(1):207–29.
[39] Bolander JE, Saito S. Fracture analyses using spring networks with random geometry. Eng Fract Mech 1998;61(5–6):569–91.
[40] Nagai K, Sato Y, Ueda T. Mesoscopic simulation of failure of mortar and concrete by 3D RBSM. J Adv Concr Technol 2005;3(3):385–402.
[41] Cusatis G, Bažant ZP, Cedolin L. Confinement-shear lattice model for concrete damage in tension and compression. I. Theory. J Eng Mech 2003;129(12): 1439–48.
[42] Cusatis G, Mencarelli A, Pelessone D, Baylot J. Lattice Discrete Particle Model (LDPM) for failure behavior of concrete. II: Calibration and validation. Cem Concr Comp 2011;33(9):891–905.
[43] Han L, Pathirage M, Akono A, Cusatis G. Lattice discrete particle modeling of size effect in slab scratch tests. J Appl Mech 2021;88:021009.
[44] Luccioni BM, Lopez DE, Danesi RF. Bond-Slip in Reinforced Concrete Elements. J Struct Engng 2005;131(11).
[45] Jendele L, Cervenka J. Finite element modelling of reinforcement with bond. Comput Struct 2006;84:1780–91.
[46] Melo J, Rossetto T, Varum H. Experimental study of bond-slip in RC structural elements with plain bars. Mater Struct 2015;48:2367–81.
[47] Dőrr K. Beitrag zur Berechnung von Stahlbetonscheiben unter Berücksichtigung des Verbundverhaltens. Darmstadt University; 1980. PhD Thesis.
[48] CEB-FIP Model Code 90. London, 1992.
[49] den Uijl JA, Bigaj A. A bond model for ribbed bars based on concrete confinement. Heron 1996;41(3):201–26.
[50] Haskett M, Oehlers DJ, Mohamed Ali MS. Local and global bond characteristics of steel reinforcing bars. Engng Struct 2008;30(2):376–83.
[51] Skarzynski L, Tejchman J. Investigations on fracture in reinforced concrete beams in 3-point bending using continuous micro-CT scanning. Constr Build Mater 2021;284:122796.
[52] Tejchman J, Kozicki J. Experimental and theoretical investigation of steel-fibrous concrete. Springer Series on Geomechanics and Geoengineering: Springer-Verlag, Berlin Heidelberg; 2010.
[53] Skarzynski L, Marzec I. Shear fracture of longitudinally reinforced concrete beams under bending using Digital Image Correlation and FE simulations with concrete micro-structure based on X-ray micro-computed tomography images. Constr Build Mater 2021;274:122116.
[54] Jin L, Liu M, Zhang R, Du X. 3D meso-scale modelling of the interface behavior between ribbed steel bar and concrete. Engng Fract Mech 2020;239:107291.
[55] Liu M, Jin L, Chen F, Zhang R, Du X. 3D meso-scale modelling of the bonding failure between corroded ribbed steel bar and concrete. Engng Struct 2022;256: 113939.
[56] Kozicki J, Donzé FV. A new open-source software developer for numerical simulations using discrete modeling methods. Comput Methods Appl Mech Engng 2008;19:4429–43.
[57] Šmilauer V, et al., Yade Documentation 3rd ed. The Yade Project. doi:10.5281/zenodo.5705394 (http://yade-dem.org/doc/), 2021.
[58] Zivaljic N, Nikolic Z, Smoljanovic H. Computational aspects of the combined finite–discrete element method in modelling of plane reinforced concrete structures. Engng Fract Mech 2014;131:669–866.
[59] Yazarlu A, Dehestani M. Application of discrete element method (DEM) in characterization of bond-slip behavior in RC beams with confinement subjected to corrosion. Structures 2020;28:1965–76.
[60] Shirzehhagh M, Fakhimi A. Insights on crack initiation and propagation in reinforced concrete beams, a bonded-particle approach. *Engineering Structure* 2021; 244:112783.
[61] Yin XJ, Zhang B, Yu QQ, Gu XL. Overturning collapse responses of RC frame-shear wall structures induced by failure of vertical members. Engng Struct 2023; 285:116078.
[62] Suchorzewski J, Korol E, Tejchman J, Mróz Z. Experimental study of shear strength and failure mechanisms in RC beams scaled along height or length. Eng Struct 2018;157:203–23.
[63] Cundall P, Strack ODL. A discrete numerical model for granular assemblies. Géotechnique 1979;29(1):47–65.
[64] Cundall P, Hart R. Numerical modelling of discontinua. Engng Comput 1992;9:101–13.
[65] Tomporowski D, Nitka M, Tejchman J. Application of the 3D DEM in the modelling of fractures in pre-flawed marble specimens during uniaxial compression. Engng Fract Mech 2023;277:108978.
[66] Nitka M, Tejchman J, Kozicki J, Leśniewska D. DEM analysis of micro-structural events within granular shear zones under passive earth pressure conditions. Granul Matter 2015;17(3).
[67] Kozicki J, Niedostatkiewicz M, Tejchman J, Mühlhaus HB. Discrete modelling results of a direct shear test for granular materials versus FE results. Granul Matter 2013, 2013,;15(5):607–27.
[68] Kozicki J, Tejchman J, Műhlhaus HB. Discrete simulations of a triaxial compression test for sand by DEM. Int J Num Anal Meth Geomech 2014;38:1923–52.
[69] Kozicki J, Tejchman J. Relationship between vortex structures and shear localization in 3D granular specimens based on combined DEM and Helmholtz-Hodge decomposition. Granul Matter 2018;20:48.
[70] Krzaczek M, Kozicki J, Nitka M, Tejchman J. Simulations of hydro-fracking in rock mass at meso-scale using fully coupled DEM/CFD approach. Acta Geotech 2020;15(2):297–324.
[71] Krzaczek M, Nitka M, Tejchman J. Effect of gas content in macro-pores on hydraulic fracturing in rocks using a fully coupled DEM/CFD approach. Int J Numer Anal Methods Geomech 2021;45(2):234–64.
[72] Marzec I, Tejchman J. Experimental and numerical investigations on RC beams with stirrups scaled along height or length. Engng Struct 2022;252:113621.
[73] Marzec I, Tejchman J, Mróz X. Numerical analysis of size effect in RC beams scaled along height or length using elasto-plastic-damage model enhanced by non-local softening. Finite Elem Anal Des 2019;157:1–20.
[74] Roux JN, Chevoir F. Discrete numerical simulation and this mechanical behavior of granular materials. *Bulletin des Laboratoires des Ponts et Chausses* 2005.
[75] Luding S. The effect of friction on wide shear bands. Journal Particulate Science and Technology 2007;26(1):33–42.
[76] Xiao J, Li W, Suc Z, Lange DA, Shah SP. SP. Properties of interfacial transition zones in recycled aggregate concrete testes by nanoindentation. Cem Concr Compos 2013;37:276–92.
[77] Kozicki J, Tejchman J, Mróz Z. Effect of grain roughness on strength, volume changes, elastic and dissipated energies during quasi-static homogeneous triaxial compression using DEM. Granul Matter 2012;14:457–68.